

On the Vibrational State-Specific Modelling of Radiating Normal-Shocks in Air

Sangdi Gu^{*}, Jiaao Hao[†] and Chih-yung Wen[‡]
The Hong Kong Polytechnic University, Kowloon, Hong Kong

A comprehensive state-to-state (StS) model for air was formed - including vibration–vibration–translation (VVT) reactions. The generated VVT reaction rates were compared to available first principles calculations and reasonable agreement was obtained. The influence of multi-quantum transitions revealed that the possible reduction on the number of VVT transitions depends on the application. The influence of VV transitions revealed that the vibrational excitation becomes too fast if VVT transitions are reduced to VT transitions, invalidating this approximation. Comparisons were made with existing NO emission measurements in the UV and mid-IR spectrum. At velocities of 3 - 4 km/s, some of the current O₂ dissociation rates may be inaccurate. At a higher velocity of 6.81 km/s, the NO mole fraction predicted by the StS model is around an order of magnitude greater than that predicted by the two-temperature model. Finally, recommendations were given on the further development of the state-to-state model.

Nomenclature

A, B	=	atomic species
c	=	mass fraction
E	=	level energy, J
f	=	final vibrational quantum number
h_0	=	total specific enthalpy, J/kg
i	=	initial vibrational quantum number

^{*} Research Assistant Professor, Department of Aeronautical and Aviation Engineering. sangdi.gu@polyu.edu.hk.

[†] Assistant Professor, Department of Aeronautical and Aviation Engineering. jiaao.hao@polyu.edu.hk. Member AIAA.

[‡] Chair Professor and Department Head, Department of Aeronautical and Aviation Engineering. cyywen@polyu.edu.hk. Associate Fellow AIAA.

k	=	Reaction rate coefficient, $\text{cm}^3\text{mole}^{-1}\text{s}^{-1}$
k_B	=	Boltzmann's constant, J/K
L	=	path length, m
M	=	collision partner in a reaction
\mathcal{M}	=	molar mass, kg/mol
n	=	number density, particles/ m^3
P	=	probability
p	=	pressure, Pa
S	=	band radiance, $\text{W}\cdot\text{m}^{-3}\cdot\text{sr}^{-1}$
T	=	translational temperature, K
T_e	=	electronic temperature, K
T_v	=	average vibrational temperature, K
u	=	velocity, m/s
\dot{w}_t	=	mass production rate, $\text{kg}/(\text{m}^3\text{s})$
X	=	molar concentration, mol/cm^3
x	=	position along flow axis, m
ρ	=	mass density, kg/m^3
$\tau_{\text{AB-M}}$	=	vibrational relaxation time, s

Subscripts

1	=	molecule 1 of a vibration–vibration–translation reaction
2	=	molecule 2 of a vibration–vibration–translation reaction
A, B	=	atomic species
AB, CD	=	diatomic species
EX	=	exchange reaction
i	=	species index
v	=	vibrational level
VT	=	vibration–translation transition

VVT = vibration–vibration–translation transition

∞ = freestream

Superscripts

eq = equilibrium

I. Introduction

Thermochemical nonequilibrium flows often occur in the flowfields of hypersonic flight vehicles, including hypersonic cruisers and capsules reentering from low Earth orbit. For air, important processes involved in these flows include vibrational excitation, molecular dissociation, and neutral exchange reactions. Particular focus is currently given to the modelling of these processes, driven by interplanetary missions involving atmospheric entries.

During hypersonic flight, high temperatures and relatively low pressures are often encountered which causes the vibrational energy mode of molecules to be in a nonequilibrium state with respect to the translation mode of heavy particles due to the lack of collisions necessary to equilibrate. The resulting nonequilibrium vibrational population distribution for N_2 and O_2 would affect dissociation, and dissociation, in turn, would affect the vibrational energy removal as well as NO formation. Such complex coupling can be adequately described by the state-specific method tracing the temporal and spatial variation of each vibrational level.

Unlike the low fidelity multi-temperature models which are more phenomenological, the state-specific method for simulating thermochemical nonequilibrium is physically consistent. The accuracy of state-specific simulations relies on the accuracy of the kinetic rates of vibration–vibration–translation (VVT) bound–bound transitions, vibration–translation (VT) bound–bound transitions, vibration–dissociation (VD) bound–free transitions and, for air, nitric oxide exchange reactions. Hence, only recently have there been reliable state-specific studies due to the application of the forced harmonic oscillator (FHO) theory and first principles for calculating the aforementioned state-specific kinetic rates [1-8]. However, the issue with these studies is that they mostly consider only pure O_2 or N_2 . For the ones that considered a $N_2:O_2$ mixture, they either did not consider VVT transitions or they did not use accurate first principles derived rates for the NO exchange reactions. The current work consequently addresses these issues by providing a state-specific study of air including VVT transitions for N_2 and O_2 , and using accurate rates for the exchange reactions. A state-specific rates database is compiled, consisting of the VVT transitions generated in this work along with

publicly available state-specific rates for the other reactions. Many of these state-specific rates have not been properly validated. Therefore, to uncover any problematic rates and assess the performance of the current model, comparisons are made with the existing radiation emission measurements which provide a window on the non-equilibrium processes. Additionally, the influence of multi-quantum VVT transitions and the validity of simplifying VVT transitions to VT transitions are assessed.

II. The numerical model

The initial post-shock condition is calculated from the Rankine–Hugoniot relations which assumes frozen chemical composition and frozen vibrational energy. The governing equations for a normal shock flow is,

$$\begin{aligned}
 \rho du + u d\rho &= 0 \\
 dp + \rho u du &= 0 \\
 dh_0 &= 0 \\
 u dc_i - \frac{\dot{w}_i}{\rho} dx &= 0
 \end{aligned} \tag{1}$$

The usual assumption of equilibration between the translational and rotational energy modes is made. The reaction processes considered in this study include VVT transitions, VT transitions, VD reactions and NO exchange reactions. The resulting species production rate can be written generally as,

$$\begin{aligned}
 \dot{w}_{i_1} = \mathcal{M}_{i_1} \left[\right. & \sum_{i_2, f_1, f_2} k_{VVT}(f_1, f_2 \rightarrow i_1, i_2) X_{f_1} X_{f_2} - k_{VVT}(i_1, i_2 \rightarrow f_1, f_2) X_{i_1} X_{i_2} \\
 & + \sum_{M, f} k_{VT}(f, M \rightarrow i, M) X_f X_M - k_{VT}(i, M \rightarrow f, M) X_i X_M \\
 & + \sum_M k_{VD}(A, B, M \rightarrow i, M) X_A X_B X_M - k_{VD}(i, M \rightarrow A, B, M) X_i X_M \\
 & + \sum_{NO(f)} k_{EX}(NO(f), N/O \rightarrow i, N_2/O_2) X_{NO(f)} X_{N/O} - k_{EX}(i, N_2/O_2 \\
 & \left. \rightarrow NO(f), N/O) X_i X_{N_2/O_2} \right] \tag{2}
 \end{aligned}$$

where each vibrational state is considered a pseudo-species. The energies of the vibrational levels for N₂, O₂ and NO used in this work are obtained from the STELLAR database [9], which are determined by solving the radial Schrödinger equation with potential curves obtained from the Rydberg-Klyning-Rees method [10]. For all reactions, the backward reaction rates are computed from detailed balancing. The current work considers five major species – N₂, O₂, N, O and NO – and ionization is not considered. Additionally, only the ground electronic state is considered for all species. This is valid as the authors of Ref. [1, 11] discussed that ionization and electronic excitation “do not play a major role in the thermochemistry” even for a shock at 8 km/s. Therefore, as the highest velocity studied in the

current work is 7 km/s, we expect that we can simulate the thermochemistry and species in the flow by considering only the ground electronic state and using a five-species air model.

Table 1. Inelastic reactions considered in this work, where $M \in \{\text{NO}, \text{O}, \text{N}\}$.

No.	Reaction	Model	Ref.
1	$\text{N}_2(i_1) + \text{N}_2(i_2) \leftrightarrow \text{N}_2(f_1) + \text{N}_2(f_2)$	FHO	This work
2	$\text{O}_2(i_1) + \text{O}_2(i_2) \leftrightarrow \text{O}_2(f_1) + \text{O}_2(f_2)$	FHO	This work
3	$\text{O}_2(i_1) + \text{N}_2(i_2) \leftrightarrow \text{O}_2(f_1) + \text{N}_2(f_2)$	FHO	This work
4	$\text{NO}(i) + \text{N}_2 \leftrightarrow \text{NO}(f) + \text{N}_2$	FHO	[9]
5	$\text{NO}(i) + \text{O}_2 \leftrightarrow \text{NO}(f) + \text{O}_2$	FHO	[9]
6	$\text{NO}(i) + M \leftrightarrow \text{NO}(f) + M$	LT	[2, 12]
7	$\text{N}_2(i) + \text{N} \leftrightarrow \text{N}_2(f) + \text{N}$	First principles	[13]
8	$\text{O}_2(i) + \text{O} \leftrightarrow \text{O}_2(f) + \text{O}$	First principles	[14]
9	$\text{N}_2(i) + \text{O} \leftrightarrow \text{N}_2(f) + \text{O}$	LT	[2, 12]
10	$\text{O}_2(i) + \text{N} \leftrightarrow \text{O}_2(f) + \text{N}$	LT	[2, 12]
11	$\text{N}_2(i) + \text{NO} \leftrightarrow \text{N}_2(f) + \text{NO}$	LT	[2, 12]
12	$\text{O}_2(i) + \text{NO} \leftrightarrow \text{O}_2(f) + \text{NO}$	LT	[2, 12]

Table 2. Dissociation/recombination and exchange reactions considered in this work, where $M \in \{\text{NO}, \text{O}, \text{N}\}$.

No.	Reaction	Model	Ref.
1	$\text{N}_2(i) + \text{N}_2 \leftrightarrow 2\text{N} + \text{N}_2$	FHO	[9]
2	$\text{O}_2(i) + \text{O}_2 \leftrightarrow 2\text{O} + \text{O}_2$	FHO	[9]
3	$\text{N}_2(i) + \text{O}_2 \leftrightarrow 2\text{N} + \text{O}_2$	FHO	[9]
4	$\text{O}_2(i) + \text{N}_2 \leftrightarrow 2\text{O} + \text{N}_2$	FHO	[9]
5	$\text{N}_2(i) + \text{N} \leftrightarrow 3\text{N}$	First principles	[13]
6	$\text{O}_2(i) + \text{O} \leftrightarrow 3\text{O}$	First principles	[14]
7	$\text{N}_2(i) + \text{O} \leftrightarrow 2\text{N} + \text{O}$	Reaction 5	[12]
8	$\text{O}_2(i) + \text{N} \leftrightarrow 2\text{O} + \text{N}$	Reaction 6	[12]
9	$\text{N}_2(i) + \text{NO} \leftrightarrow 2\text{N} + \text{NO}$	Reaction 1	[12]
10	$\text{O}_2(i) + \text{NO} \leftrightarrow 2\text{O} + \text{NO}$	Reaction 4	[12]
11	$\text{NO}(i) + \text{N}_2 \leftrightarrow \text{N} + \text{O} + \text{N}_2$	FHO	[9]
12	$\text{NO}(i) + \text{O}_2 \leftrightarrow \text{N} + \text{O} + \text{O}_2$	FHO	[9]
13	$\text{NO}(i) + M \leftrightarrow \text{N} + \text{O} + M$	(Reaction 11) x 20	[12]
14	$\text{N}_2(i) + \text{O} \leftrightarrow \text{NO}(f) + \text{N}$	First principles	[15]
15	$\text{O}_2(i) + \text{N} \leftrightarrow \text{NO}(f) + \text{O}$	First principles	[16]

The VVT and VT reactions considered in the current work is listed in Table 1. Reactions 1-3 are the VVT reactions considered in the current work, with the rates generated in this work using the FHO theory (see Supplementary Materials for details of the FHO theory). All other FHO rates in the table are obtained from the STELLAR database [17]. Reactions 7 and 8 are the VT reaction of N_2 and O_2 colliding with N and O respectively for which the rates are obtained from first principles [13, 14]. No state-specific rates are available for reactions 6 and 9 - 12, thus, the classic Landau-Teller (LT) model in StS form is applied, derived by Ref. [2],

$$k_{VT} = \frac{1}{X_M} \left(\frac{c_{ABv}}{c_{AB}} \right)^{eq} \frac{1}{\tau_{AB-M}} \quad (3)$$

with the vibrational relaxation time, τ_{AB-M} , calculated according to Park [12].

The dissociation and exchange reactions considered in this work are listed in Table 2. All FHO rates in the table are obtained from the STELLAR database [10, 17]. Reactions 5 and 6 are the dissociation reaction of N_2 and O_2 colliding with N and O respectively for which the rates are obtained from first principles [13, 14]. For reactions 14 and 15, the state-specific NO exchange reaction rates are obtained from the first principles calculation of Ref. [15, 16], which have been rigorously assessed with respect to experimental and other theoretical results [2, 18-20]. Order of magnitude agreements were observed, though the present rates were shown to be consistently slower than some of the other results [18-20], which led to lower post-shock peak NO mole fractions as shown in Ref. [2]. For the dissociation reactions where no state-specific rates are available, the concept of third body efficiencies is applied using the efficiencies given by Park [12], which is a common approximation [19].

III. Validation of the forced harmonic oscillator model

Unlike first principles calculations which make use of the analytical representation of potential energy surfaces (PES) to simulate large numbers of collisions through classical or semi-classical mechanics to obtain reaction rate coefficients [21], the FHO theory is a semiclassical nonperturbative analytic method which allows the accurate calculation of VT and VVT transition probabilities for a harmonic oscillator acted upon by an external exponential force [22]. In this theory, it is assumed that VT and VVT transitions occur as a series of virtual one-quantum jumps during a collinear collision. Various corrections are incorporated to account for anharmonicity, noncollinear collisions, and detailed balance [10]. The formulation of the FHO theory is well documented, for example in Ref. [9, 10, 22-27], thus, it is not repeated here (see Supplementary Materials for details).

Numerous works have used the FHO theory to generate VVT, VT and VD transition rates to model thermochemical nonequilibrium, yielding good results [2, 9, 10, 25, 26, 28-32]. Further validation of the FHO theory using both the Morse and purely repulsive intermolecular potentials is provided in this work for VVT transitions by comparison to available first principles calculation and experimental data. Simplified expressions exist for the evaluation of the FHO probabilities to overcome issues with numerical singularities, overflows and underflows encountered when computing transitions between high vibrational quantum numbers [10]. The accuracy of these approximate expressions is assessed here when used with the purely repulsive intermolecular potential.

The FHO O_2 - O_2 VVT rates are compared with semi-classical (SC) first principles calculations from Ref. [33-35] and experimental data from Ref. [36]. Some of the results are shown in Fig. 1 (see Supplementary Materials for more). Particularly good agreement is observed for the $O_2(i_1) + O_2(0) \rightarrow O_2(i_1-1) + O_2(0)$ VT process, with Fig. 1 (a) showing an example. Additionally, the use of the approximate expression for the FHO probabilities seems to be remarkably accurate for these VT transitions. For the $O_2(i_2-1) + O_2(1) \rightarrow O_2(i_2) + O_2(0)$ VV process, the agreement with the SC results is generally good at around 1000 K but poor at temperatures close to 100 K, with Fig. 1 (b) showing an example, though temperatures close to 100 K are irrelevant for nonequilibrium post-shock flows. The obvious anti-Arrhenius behavior observed at the low temperatures is expected and it can only be captured by first principles calculation. Also, for this transition, significant differences between the full and approximate expressions for the FHO probabilities appear at temperatures between 10,000 K and 100,000 K. The $O_2(i_1) + O_2(0) \rightarrow O_2(i_1-2) + O_2(0)$ VT process, $O_2(i_1) + O_2(i_2 = i_1) \rightarrow O_2(i_1+2) + O_2(i_2-2)$ VV process, $O_2(i_1) + O_2(i_2) \rightarrow O_2(i_1-1) + O_2(i_2-1)$ VVT process, and $O_2(i_1) + O_2(i_2) \rightarrow O_2(i_1-2) + O_2(i_2-2)$ VVT process were also assessed and agreement to within a factor of 3 with the SC results is generally observed for lower vibrational levels (≤ 5) at higher temperatures (≥ 4000). Lastly, in general, the purely repulsive and Morse intermolecular potential produce FHO results which agree to within an order of magnitude, with more noticeable differences appearing only at very low temperatures (< 300 K), which is irrelevant for nonequilibrium post-shock flows.

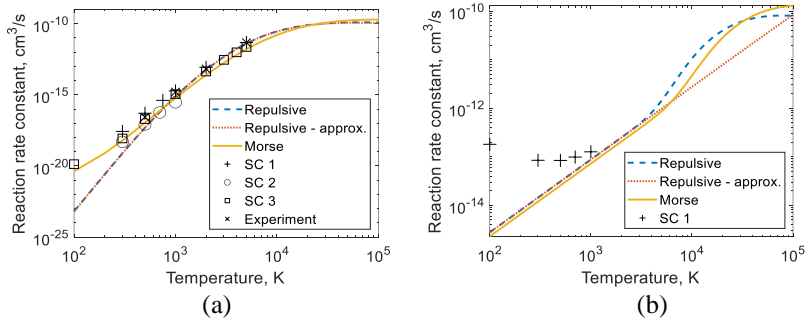


Fig. 1. Reaction rate coefficients for the (a) $O_2(1) + O_2(0) \rightarrow O_2(0) + O_2(0)$ VT process and (b) $O_2(1) + O_2(0) \rightarrow O_2(0) + O_2(1)$ VV process. SC 1, SC 2 and SC 3 is from Ref. [33], [34] and [35] respectively, while experiment is from [36].

The FHO N_2 - N_2 VVT rates are compared with semi-classical (SC) first principles calculations from Ref. [37, 38]. Assessed were the $N_2(i_1) + N_2(i_2) \rightarrow N_2(i_1-n) + N_2(i_2)$ VT process and the $N_2(i_1) + N_2(i_2) \rightarrow N_2(i_1+n) + N_2(i_2-n)$ VV process, with $n = 1$ or 2 . Some of the results are shown in Fig. 2 (see Supplementary Materials for the rest). Order of

magnitude agreement is generally achieved at temperatures beyond 2000 K. The cases shown in Fig. 2 has particularly good agreement, within a factor of 2. In general, the agreement with SC results improves with increasing temperature, which is important for post-shock nonequilibrium flows. In most cases, the approximate expression for the FHO probabilities seems to be accurate. Notable differences between the full and approximate expressions appear between 10,000 K and 100,000 K for the VV processes. Lastly, just like with the O₂-O₂ encounter, the purely repulsive and Morse intermolecular potential produce N₂-N₂ FHO results which agree to within an order of magnitude.

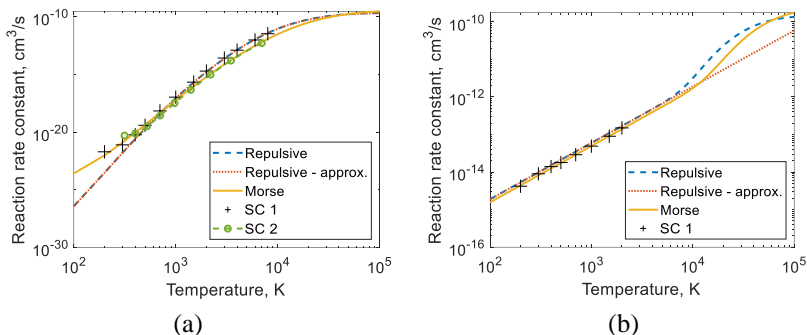


Fig. 2. Reaction rate coefficients of (a) $N_2(1) + N_2(0) \rightarrow N_2(0) + N_2(0)$ and (b) $N_2(0) + N_2(1) \rightarrow N_2(1) + N_2(0)$. ‘SC 1’ and ‘SC 2’ are from Ref. [37] and [38] respectively.

The FHO O₂-N₂ VVT rates are compared with semi-classical (SC) first principles calculations from Ref. [39, 40], quasi-classical trajectory (QCT) first principles calculations from Ref. [41, 42], and experiment of Ref. [43]. Assessed were the O₂(0) + N₂(1) → O₂(1) + N₂(0) VV process, O₂(i₁) + N₂(i₂) → O₂(i₁-1) + N₂(i₂+1) VV process, O₂(i₁) + N₂(i₂) → O₂(i₁-1) + N₂(i₂) VT process, and the O₂(0) + N₂(1) → O₂(0) + N₂(0) VT process. Some of the results are shown in Fig. 3 (see Supplementary Materials for the rest). Order of magnitude agreement is generally observed at temperatures beyond 8000 K and improves with increasing temperature. In many cases, such as the O₂(13) + N₂(0) → O₂(12) + N₂(1) VV process, the O₂(22) + N₂(0) → O₂(21) + N₂(1) VV process, and the O₂(0) + N₂(1) → O₂(0) + N₂(0) VT process, order of magnitude agreement is observed even at lower temperatures around 1000 K. Regarding the O₂(0) + N₂(1) → O₂(0) + N₂(0) VT process shown in Fig. 3 (b), considerable discrepancy appears between the SC and QCT results at lower temperatures of around 2000 K. This could be attributed to the failure of the QCT method at lower temperatures due to the pronounced quantum effects [42]. The SC method, like the QCT method, makes use of PES to perform collision simulations, with the difference being the collisions are treated semi-classically in the SC method which involves additional time-dependent Schrödinger equations. Regarding the O₂(0) + N₂(1) → O₂(1) + N₂(0) VV process shown in Fig. 3 (a), large discrepancies exist between the experimental measurements and the first principles

calculations at lower temperatures, with the FHO results agreeing very closely with the experimental measurements. In this case, it is unclear what the issue is and which are the correct rates. Lastly, comparing the results from the full and approximate FHO probability expressions, distinct differences appear beyond 10,000 K for the VV processes, while the purely repulsive and Morse intermolecular potential produce FHO results which agree to within an order of magnitude.

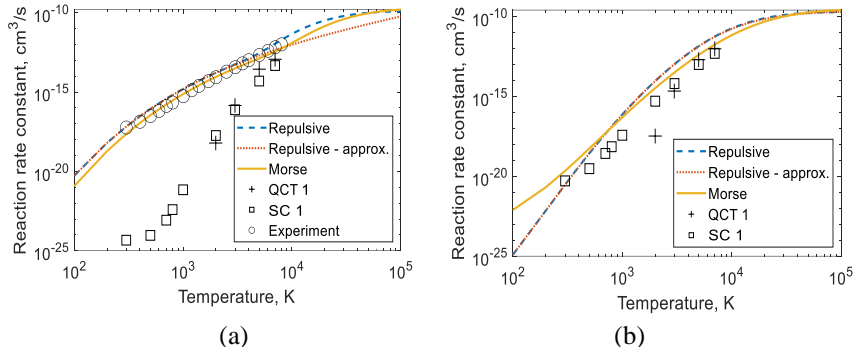


Fig. 3. Reaction rate coefficients of the (a) $\text{O}_2(0) + \text{N}_2(1) \rightarrow \text{O}_2(1) + \text{N}_2(0)$ VV process and (b) $\text{O}_2(0) + \text{N}_2(1) \rightarrow \text{O}_2(0) + \text{N}_2(0)$ VT process. The ‘QCT 1’ data is from Ref. [42], while the ‘SC 1’ data is from Ref. [40]. The experimental data is from Ref. [43].

In general, the FHO results agree reasonably well with the first principles calculation and experimental data, particularly at higher temperatures which are important for post-shock nonequilibrium simulations. The FHO results are not particularly sensitive to which intermolecular potential is used, hence the purely repulsive intermolecular potential is used in the current work. The simplified expressions for the evaluation of FHO probabilities perform well most of the time. Though in several VV cases, the simplified expression can overestimate the reaction rate by around an order of magnitude at higher temperatures, which has been mentioned by Ref. [23]. Consequently, these expressions are used in the current work only when numerical singularities, overflows and underflows are encountered when using the original FHO probability expressions.

IV. Characteristics of VVT transitions

A. Influence of multi-quantum transitions in VVT transitions

State-to-state (StS) modelling, particularly ones where VVT transitions are modeled, generally involves huge amounts of reactions. This is a computational issue, with the bottleneck being the evaluation of the master equation [44]. As a result, its use in multi-dimensional Navier-Stokes solvers is prohibited. In general, the probability of transition decreases with increasing magnitude of the quantum transition. The transition rates between two quantum

levels very far apart may be so small as to be considered negligible. Therefore, it is of interest to investigate this for VVT transitions for the possibility of reduced order modelling and improving computational time.

Three numerical test conditions, denoted ‘N1’, ‘N2’ and ‘N3’ as shown in Table 3, are simulated for this study. The freestream pressure, temperature and N₂:O₂ mole fraction remain constant with the conditions of 300 Pa, 300 K and 0.78:0.22, respectively, while the freestream velocity varies from 3 km/s to 7 km/s. As the VVT reactions dominate the contribution to the total number of reactions, multi-quantum restrictions are applied to these reactions. The multi-quantum transition rules tested are shown in Table 4 along with the corresponding number of VVT transitions. Cases ‘L1’ to ‘L4’ tests the influence of N₂ multi-quantum transitions while cases ‘L5’ to ‘L8’ tests the influence of O₂ multi-quantum transitions. Additionally, case ‘L9’ considers all possible quantum transitions while case ‘L10’ considers only single-quantum transitions.

Table 3. Numerical test conditions.

Condition	Freestream velocity u_∞ , km/s	Frozen post-shock pressure, kPa	Frozen post-shock temperature, K
N1	3.0	26.01	4626
N2	5.0	72.34	12348
N3	7.0	141.83	23930

Table 4. Level based multi-quantum transition cases

Case	Δv_{\max} O ₂	Δv_{\max} N ₂	No. of VVT transitions
L1	All	35	2.0×10^7
L2	All	25	1.5×10^7
L3	All	15	1.0×10^7
L4	All	5	6×10^6
L5	35	All	2.5×10^7
L6	25	All	2.3×10^7
L7	15	All	2.0×10^7
L8	5	All	1.6×10^7
L9	All	All	2.6×10^7
L10	1	1	6.7×10^4

For all the tested freestream conditions, all the tested multi-quantum restrictions except for the single-quantum transition case (L10) produced minimal (less than 3 %) influences to the post-shock pressure, velocity, translational temperature and density profiles. An example of this is shown in Fig. 4 for the temperature and density profile of the N3 test case. It can also be observed that these macroscopic fluid properties are more sensitive to the multi-quantum restrictions for N₂ compared to O₂, and this is mainly because the gas mixture contains significantly more N₂ than O₂.

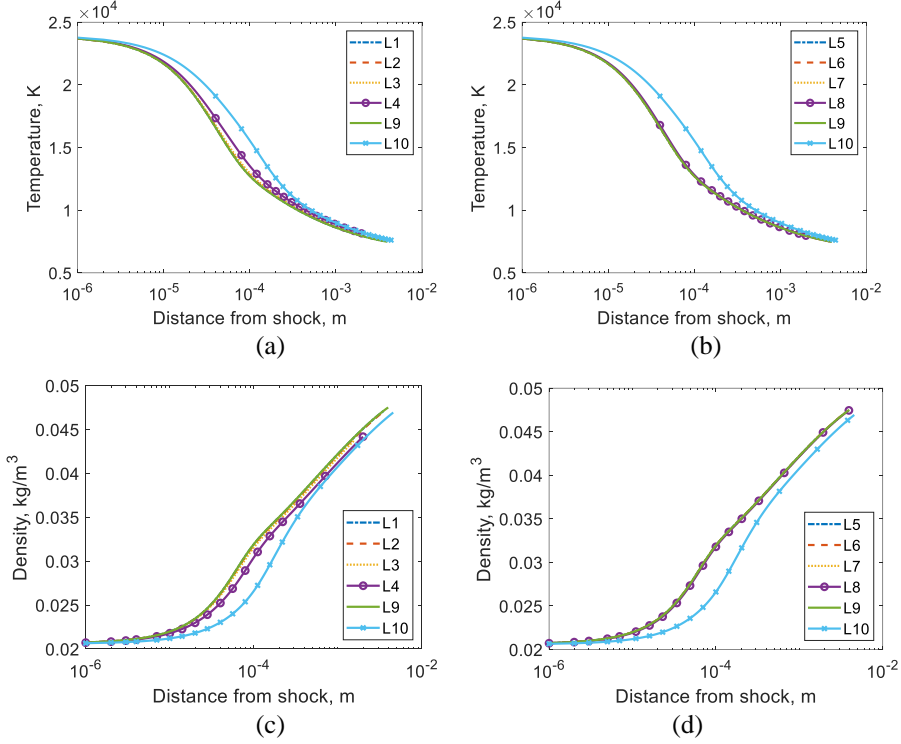


Fig. 4. Influence of multi-quantum transitions on the temperature and density profile of the N3 test case. The L1 to L4 and L5 to L8 cases represent the influence of N_2 and O_2 multi-quantum transitions respectively.

To further assess the influence of multi-quantum restrictions, the vibrational energy of N_2 , O_2 and NO per unit mass of the gas mixture is analyzed. As this is the species vibrational energy per unit mass of the mixture, its value depends on the vibrational energy distribution as well as the species mass fraction. The results are shown in Fig. 5 for O_2 . For the 3.0 km/s and 5.0 km/s conditions, all the tested multi-quantum restrictions except for the single-quantum transition case (L10) produced minimal influences on the vibrational energy profile, as is the case with the density profile. For the 7.0 km/s condition, influences from the multi-quantum restriction of 5 become observable, showing that the influence of multi-quantum restrictions is dependent on the freestream condition – the influence increases with increasing total enthalpy. As Fig. 5 shows the O_2 vibrational energy, the influence is more pronounced when this restriction is applied to O_2 quantum jumps (L8) but it is still observable when applied to N_2 quantum jumps (L4) due to the existing coupling between the two molecules. The same trend is observed for N_2 . Regarding the NO vibrational energy, for the 3.0 km/s, restrictions as small as 5 quanta produce negligible influence. The influence is more obvious for the 5.0 km/s and 7.0 km/s conditions, as shown in Fig. 6, where a difference of almost 10 % can be seen when the quantum jump of N_2 is restricted to 5 (L4) for the 7 km/s case. For the 5 km/s case, restrictions to 5 quanta in N_2 and

O_2 produced similar influences to the NO vibrational energy. On the other hand, for the 7 km/s case, the restriction in N_2 is significantly more influential compared to the restriction in O_2 due to the rapid complete dissociation of O_2 .

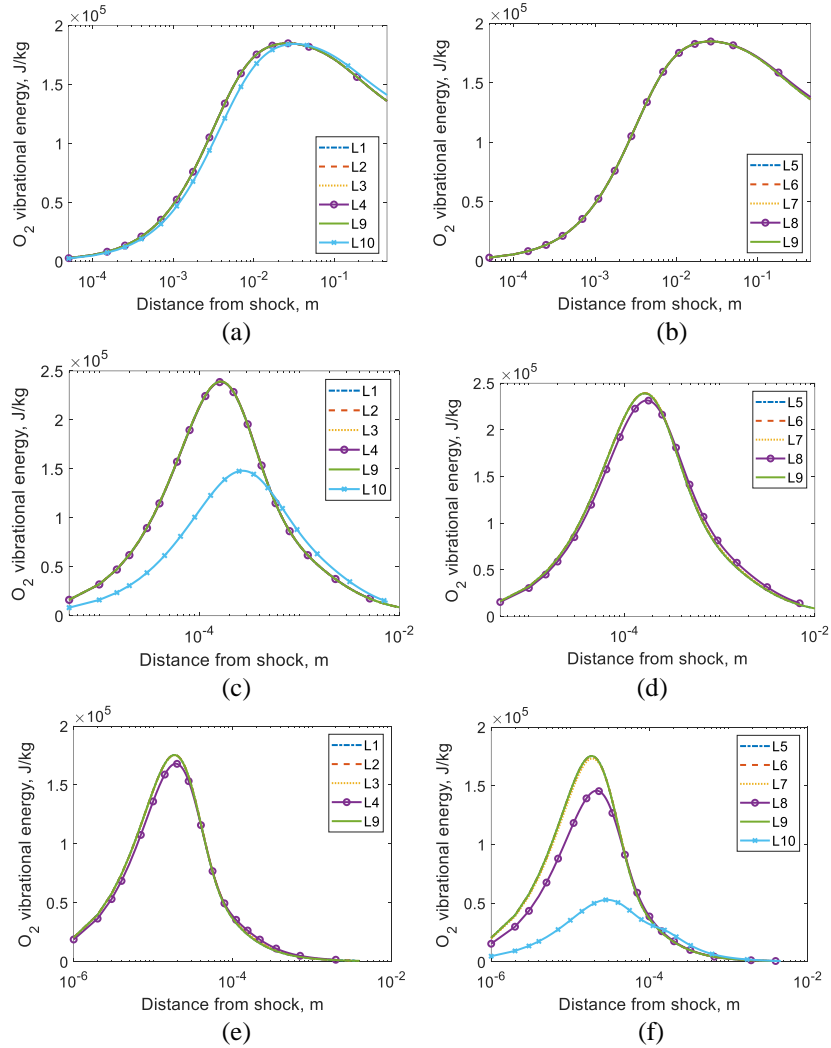


Fig. 5. The O_2 vibrational energy per kg of gas mixture. The top ((a) and (b)), middle ((c) and (d)) and bottom ((e) and (f)) rows correspond to the N1, N2 and N3 freestream conditions respectively.

Concerning the vibrational population distribution of the molecular species, obvious influence of multi-quantum transitions is observed in the strong non-equilibrium conditions close to the shock front. The results are shown in Fig. 7 with the plots extracted at 3.4×10^{-3} m, 2×10^{-4} m, and 6×10^{-6} m behind the shock front for the 3.0 km/s, 5.0 km/s and 7.0 km/s conditions respectively. Orders of magnitude differences in O_2 and N_2 can be observed in the population of the higher energy levels, even for the 3.0 km/s condition, when quantum jump restrictions are applied on the respective molecules. These differences are not reflected in vibrational energy plots, such as those shown in Fig. 5, because the population of the higher energy levels is too low to significantly influence the vibrational energy. As can

be seen in Fig. 7, the influence of multi-quantum restrictions increases and extends towards the lower energy levels as the freestream velocity increases, but it is still not enough to influence the vibrational energy to orders of magnitude extent. The influence of multi-quantum restrictions disappears at locations further downstream of the shock front as the flow equilibrates. Regarding the vibrational population distribution of NO, it is uninfluenced by any quantum jump restrictions to N_2 and O_2 , not only at the plotted location in Fig. 7 but at any location behind the shock. This is understandable because the current state-specific study, as well as past state-specific studies, revealed that NO forms at excited vibrational states and, thus, does not need to climb the vibrational ladder as is required for N_2 and O_2 [2, 27, 45, 46]. This means that NO is never in a strong nonequilibrium or non-Boltzmann vibrational state anywhere behind the shock at any freestream condition. As a result, the NO vibrational population distribution is robust and uninfluenced by different vibrational excitations of N_2 and O_2 . A high-fidelity model for the NO vibrational excitation process is, thus, less important because NO forms in vibrationally excited states already. The differences of the NO vibrational energy profiles shown in Fig. 6 is mainly driven by the differences in NO mass fraction.

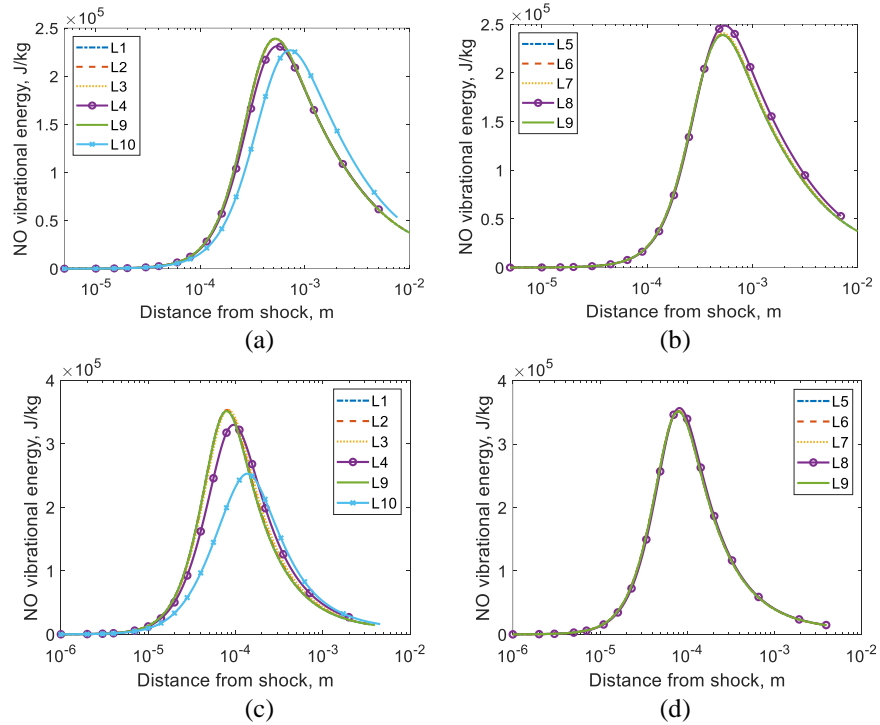


Fig. 6. The NO vibrational energy per kg of gas mixture. The top ((a) and (b)) and bottom ((c) and (d)) rows correspond to the N2 and N3 freestream conditions respectively.

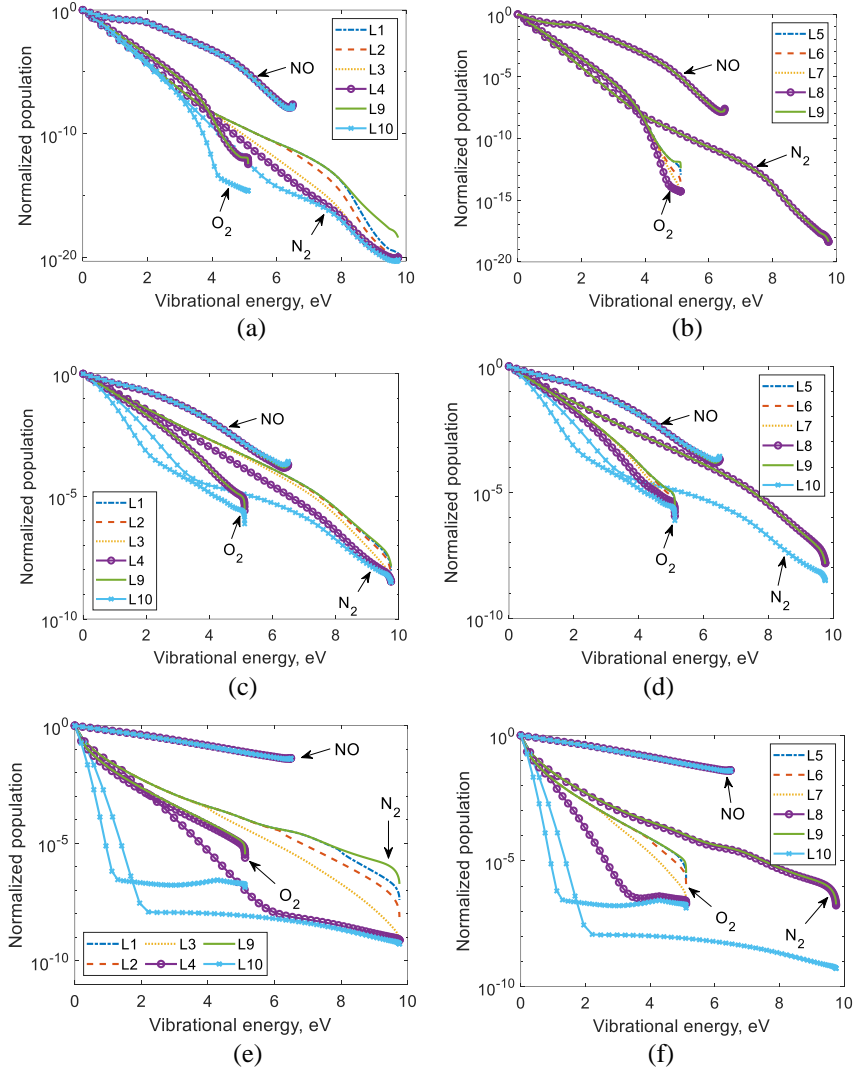


Fig. 7. The normalized vibrational population distributions. The top ((a) and (b)), middle ((c) and (d)) and bottom ((e) and (f)) rows correspond to the N1, N2 and N3 freestream conditions respectively. The plots are extracted at 3.4×10^{-3} m, 2×10^{-4} m, and 6×10^{-6} m behind the shock front for the N1, N2 and N3 conditions respectively.

In addition to the discussed quantum energy level-based approach to restricting the multi-quantum jumps, another approach involves restricting the quantum jumps based on the absolute energy difference between the quantum levels involved in the transition. To compare with the L4 and L8 test cases, two test cases is created, denoted E1 and E2 respectively, based on restricting the energy change of the transition and matching the number of transitions. As shown in Table 5, this involves restricting the possible quantum jumps to less than or equal to 0.62 eV. The result showed that in all cases, the level-based criteria gives a better result than the energy-based criteria for the same number of transitions.

The result for the 7.0 km/s is shown in Fig. 8. Looking at the density shown in Fig. 8 (a), the result from the E1 test case is almost as poor as that from the L10 test case despite allowing significantly more transitions – 6.0×10^6 versus 6.7×10^4 . Looking at the species vibrational energy per mass of gas mixture shown in Fig. 8 (b) and (c), both of the energy-based cases give a poorer result compared with the corresponding level-based cases which contain the same number of transitions. The application of the energy-based criteria on N_2 seems particularly bad, as shown in Fig. 8 (b), where the E1 curve is closer to the L10 curve than the L4 curve. The poor performance of the energy-based criteria is also observed in the vibrational population distributions, shown in Fig. 8 (d). From the N_2 vibrational population distribution, it can be seen that significant discrepancies with the full VVT model (L9) exists even at lower energy levels and the overall distribution is close to that of the single-quantum transition test case. The same finding was made by Ref. [47] for pure N_2 in a heat bath using QCT transition rates. They mentioned that the level-based criteria providing better results is logical because it “spreads the number of state transitions considered evenly through the vibrational state space where as the energy-based criteria increases the number of state transitions at the higher energy levels at the cost of the number of state transitions carried out at lower energy levels”. Since the population of the higher energy levels is significantly lower than the population of the lower energy levels, it is incorrect to prioritize the transitions involving the higher energy levels because the absolute rates of these transitions are very low. A related finding was made by Ref. [30] who studied the multi-quantum VT transitions of pure N_2 behind a shock. They mentioned that “all vibrational states are influenced by multi-quantum processes, but the effective number of transitions decreases inversely according to the vibrational quantum number”. In light of this finding, it makes sense that the energy-based criteria produce poorer results as it goes against this finding by allocating more transitions to the higher energy levels.

Table 5. Energy based multi-quantum transition cases

Case	$\Delta\epsilon_{\max} O_2$, eV	$\Delta\epsilon_{\max} N_2$, eV	No. of VVT transitions
E1	All	0.62	6.0×10^6
E2	0.62	All	1.6×10^7

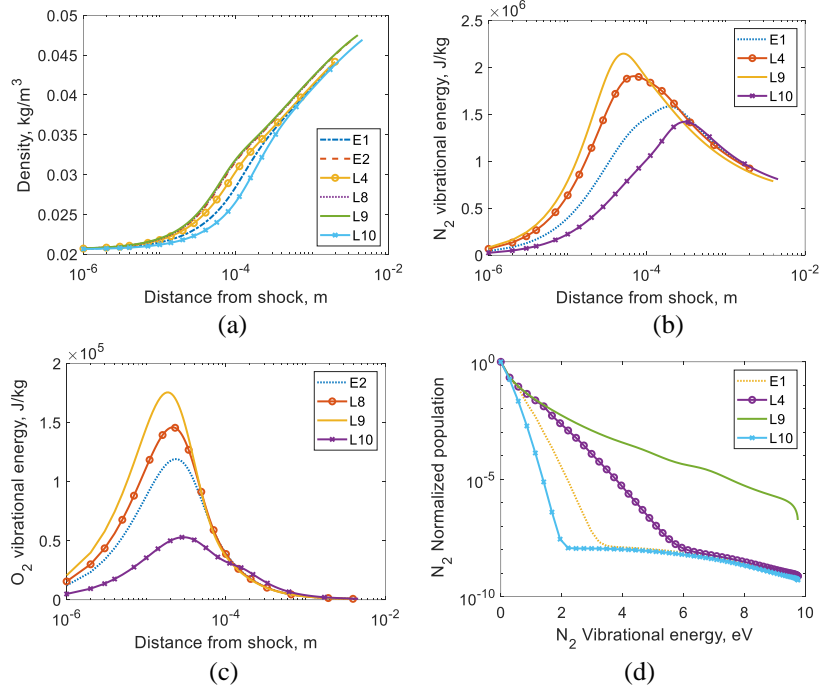


Fig. 8. Influence of multi-quantum transitions for the energy-based test cases for the N3 freestream condition on the (a) density, (b) N₂ vibrational energy, (c) O₂ vibrational energy, and (d) N₂ population distribution. The species vibrational energy shown is per kg of gas mixture. Population plot extracted at 6 μm behind the shock front.

B. Influence of vibration-vibration transitions

To reduce the number of transitions involved, as an alternative to restricting the quantum jumps of the VVT reactions, one may assume that the VVT processes occur as two independent VT processes such that the corresponding probability is given by [22, 23],

$$P(i_1, i_2 \rightarrow f_1, f_2) \approx P(i_1 \rightarrow f_1)P(i_2 \rightarrow f_2) \quad (4)$$

Summing over all of the possible vibrational states of the collision partner molecule,

$$P(i_1, \text{all} \rightarrow f_1, \text{all}) \approx P(i_1 \rightarrow f_1) \quad (5)$$

the VVT transitions reduce to VT transitions equivalent to that of molecule-atom collisions. The validity of this reduced order modelling is assessed in this section for post-shock conditions for the freestream conditions listed in Table 3.

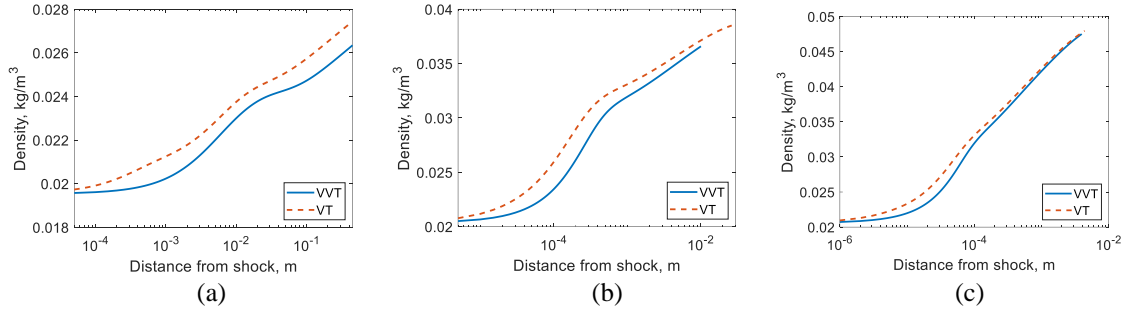


Fig. 9. Influence of VVT transitions on the post-shock density profile for the (a) N1, (b) N2, and (c) N3 test cases.

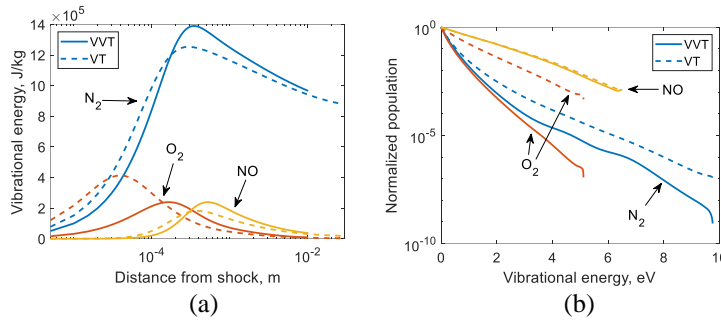


Fig. 10. Influence of VVT transitions on the (a) species vibrational energy per unit mass of mixture, and (b) species vibrational population distribution for the N2 test case. The population distribution is extracted at 30 μm behind the shock.

The results show that in general, the reduction of VVT transitions to VT transitions is a poor approximation for all the conditions tested. As shown in Fig. 9, significant discrepancies in the post-shock density profiles can be observed. The agreement does seem to improve with increasing freestream velocity (post-shock temperature) though, which is consistent with the finding of Ref. [22]. When assessing the species vibrational energy per unit mass of mixture, significant discrepancies are again observed. In all cases, significantly faster vibrational excitation and earlier dissociation is seen in both N_2 and O_2 from the VT results. An example from the 5.0 km/s condition is shown in Fig. 10 (a). This result is consistent with the result of Ref. [25] who made the same finding for a pure O_2 test gas. As a consequence, the NO vibrational energy profile is also influenced due to the altered NO formation and destruction process. The higher peak NO vibrational energy seen in the VVT result is the consequence of a higher NO mass fraction caused by the slower O_2 excitation and dissociation which leads to a higher temperature at any given position behind the shock. As explained by Ref [48], this higher temperature changes the rate and equilibrium constant of the NO exchange reactions. Lastly, as would be expected, the vibrational population distribution is significantly different between the VVT and VT results at all velocities. An example is shown in Fig. 10 (b), extracted at 30 μm behind the shock, for the 5.0 km/s condition. Large differences are observed even at the lower energy levels for both N_2 and O_2 .

The differences seen for O_2 is particularly large, which is also observed in the vibrational energy plot, which indicates that the VT approximation of VVT transitions is especially poor when applied to O_2 .

V. Comparison with experiments

There is currently a lack of validation data available for post-shock air flows. Nevertheless, there does exist measurements of post-shock radiation emission which would provide a window on the non-equilibrium processes. Treanor et al. [49] took filtered – 5.0 μm to 5.5 μm – NO mid-IR radiation (originating from ro-vibrational transitions) along a line-of-sight through a 7.62 cm inner diameter shock tube. To assess the state-specific model described in section II, the test conditions are simulated using the complete VVT model. For comparison, simulation is also carried out using the one-temperature (1T) model and the two-temperature (2T) model. The rates of Gupta [50] and rates of Park [12] are used with the 1T and 2T model respectively, which are the most popular configurations. To calculate the radiation emission, SPARK (Simulation Platform for Aerodynamics, Radiation and Kinetics) is used. SPARK is a line-by-line numerical code which calculates the spectral-dependent emission and absorption coefficients of a gas which can be in thermochemical nonequilibrium [51]. The code offers the capability of direct inputs for the populations for the internal levels of atomic and molecular species, supplied by StS codes. This is limited to vibronic levels, with rotational levels assumed to follow a Boltzmann distribution. The results are shown in Fig. 11 for nine particular conditions with properties shown in Table 6. Results from the three sets of $N_2:O_2$ mixture ratios are presented – 0.6:0.4, 0.777:0.223, and 0.95:0.05 – with nominal velocities of 3.0, 3.5 and 3.9 km/s. The freestream static pressure and temperature is 2.25 torr and 300K respectively for all these conditions. The experimental results were given with the emission coefficient as the intensity, neglecting self-absorption. Simulations using SPARK indicated this is indeed valid for these test conditions. Therefore, consistent with the experimental data, the results in Fig. 11 are given with the emission coefficient as the intensity.

Table 6. NO mid-IR experimental test conditions [49].

Condition	Freestream velocity u_∞ , km/s	Mole fraction $N_2:O_2$	Frozen post-shock pressure, kPa	Frozen post-shock temperature, K	Label in Fig. 11
EX1	3.06	0.6:0.4	27.74	4914	(a)
EX2	2.99	0.777:0.223	25.85	4599	(d)
EX3	2.97	0.95:0.05	24.89	4440	(g)
EX4	3.47	0.6:0.4	35.68	6238	(b)
EX5	3.52	0.777:0.223	35.84	6265	(e)
EX6	3.49	0.95:0.05	34.39	6023	(h)
EX7	3.85	0.6:0.4	43.94	7614	(c)
EX8	3.85	0.777:0.223	42.88	7439	(f)
EX9	3.87	0.95:0.05	42.30	7341	(i)

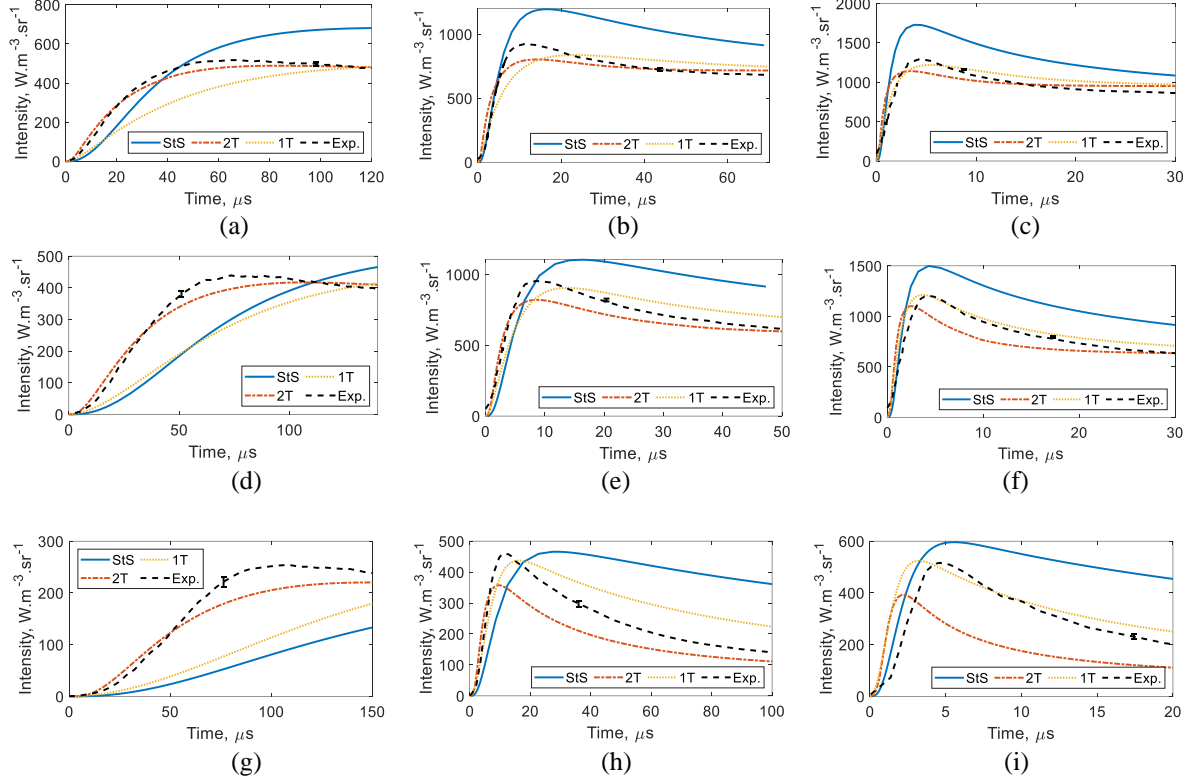


Fig. 11. Comparison of the state-to-state (StS), two-temperature (2T), and one-temperature (1T) models with experimental measurements for the post-shock NO mid-IR radiation emission for conditions (a) EX1, (b) EX4, (c) EX7, (d) EX2, (e) EX5, (f) EX8, (g) EX3, (h) EX6, (i) EX9. Error bars represent noise.

Comparing the state-specific results with the experimental results, the state-specific results generally overpredict the radiation. This is due to the higher NO mole fraction predicted in the state-specific simulations as shown in Fig. 12 (a) for the EX4 condition. On the other hand, the NO vibrational temperature is less important in these cases. The vibrational temperatures in the StS simulations are obtained by solving the following equation for $T_{v,AB}$,

$$\sum_{v=0}^{v_{max}(AB)} \frac{\rho_{ABv}}{\rho_{AB}} E_{ABv} = \frac{\sum_{v=0}^{v_{max}(AB)} E_{ABv} \exp\left(-\frac{E_{ABv}}{k_B T_{v,AB}}\right)}{\sum_{v=0}^{v_{max}(AB)} \exp\left(-\frac{E_{ABv}}{k_B T_{v,AB}}\right)} \quad (6)$$

where the energy of the nonequilibrium vibrational distribution equals the energy of a Boltzmann equilibrium vibrational distribution at a vibrational temperature. Quantitatively, the mole fraction profile shown in Fig. 12 (a) matches with the radiation profile shown in Fig. 11 (b) with only a small influence from the NO vibrational temperature profile shown in Fig. 12 (b). The lack of influence of the vibrational temperature is most obvious in the EX3 condition. The StS predicted radiation, in Fig. 11 (g), is lower than that of the 1T and 2T results throughout the test time even though the corresponding StS NO vibrational temperature, shown in Fig. 13 (c), is greater than the 1T

and 2T vibrational temperatures. The StS NO vibrational temperature is significantly higher than the 1T and 2T vibrational temperatures due to the state-specific formation of NO at vibrationally excited states as discussed earlier. The radiation is, thus, governed more by the NO mole fraction and the same trend is observed for the other conditions. Indeed, this result is obvious from a visual inspection of the empirical formula for computing the NO mid-IR band radiance under thermal equilibrium [1],

$$S = 1.29 \times 10^{-26} n_{NO} L [1 + 1.31 \times 10^{-4} (T - 3000)] \quad (7)$$

as n_{NO} and T have the same exponent. Nevertheless, the influence of the higher vibrational temperature in the StS simulation is still observable for the EX3 condition as the relative difference in radiation between the 1T and StS case is smaller than the relative difference in NO mole fraction. Also observable in the EX3 result is the significant underprediction of the rate of increase of radiation by the StS model which is not observed for the other conditions.

To explain the major discrepancies between the StS results and experimental measurements, it is necessary to consider the mechanisms of the formation and destruction of NO. For these test conditions, the main reactions influencing NO mole fraction is the O_2 dissociation reaction, NO dissociation reaction, and the $N_2 + O \leftrightarrow NO + N$ exchange reaction [1, 52]. The rapid dissociation of O_2 generates the O atoms which drives the formation of NO through the aforementioned exchange reaction. In most cases, NO forms in quantities that exceed the final post-shock equilibrium mole fraction while the equilibrium of this exchange reaction favors the formation of NO over N_2 resulting in the existence of a peak NO mole fraction. The dissociation reaction of NO helps destroy the excess NO created via exchange, and therefore can influence both the peak NO mole fraction as well as the relaxation towards equilibrium NO mole fraction. As mentioned earlier, the state specific exchange reaction rates used in this work has been rigorously assessed with experimental and theoretical results [2, 18-20]. Order of magnitude agreements were observed, though the present rates were shown to be consistently slower than some of the other results [18-20], which led to lower post-shock peak NO mole fractions as shown in Ref. [2]. Hence, while it is acknowledged that the NO exchange reactions are important and the rates differ greatly amongst different sources which can significantly influence the post-shock NO mole fraction profile, the choice of using the current NO exchange rates probably cannot explain the overprediction of the NO mole fraction seen in the current results. Nevertheless, a future study using exchange rates from many different sources will be conducted to confirm this. Thus, for the current work a sensitivity study is performed on the other reactions (which have never been assessed rigorously), using the EX4 condition as an example. The result is plotted in Fig. 14 (a) showing the effect of increasing the species dissociation and vibrational

excitation rate by a factor of 10. Unsurprisingly, it is found that the N_2 vibrational excitation and dissociation is uninfluential at the current conditions. The NO dissociation is also found to have little influence on the NO mole fraction, although Ref. [52] showed it has a major effect at 8 km/s. For the current conditions, the key reactions influencing the NO mole fraction is found to be the O_2 dissociation reactions and, in turn, the O_2 vibrational excitation reactions which influence the O_2 dissociation through coupling. Of these two reactions, it is the O_2 dissociation rates which are most likely the cause of the discrepancies. Although both are generated from FHO (apart from the O_2 -O dissociation rate which is from QCT), this theory was formulated for computing VT and VVT rates only, with reasonable (at least order of magnitude) agreement with first principles calculations as shown in section III. Additionally, the NO mole fraction is very sensitive to the O_2 VD rates as shown in Fig. 14 (a). As illustrated in Fig. 14 (a) and discussed in section IV.B, a faster O_2 dissociation leads to a lower NO peak meaning that the O_2 dissociation rates used in this work is likely too slow. Recent comparisons with some QCT calculations showed that the FHO rates for the O_2 VD reaction were indeed slow, by up to an order of magnitude, with O_2 as the collision partner [53]. Conflicting results do exist where the FHO O_2 dissociation rates were shown to be too fast when compared to experiments and QCT simulations [8, 25, 28]. However, these results were obtained for temperatures closer to 10,000 K while the current analysis concerns temperatures of around 5,000 K, and some of these results were for pure oxygen only. Due to the sensitivity of the NO mole fraction to the O_2 VD reactions as shown in Fig. 14 (a), errors in the O_2 VD rates would be particularly obvious in the NO mid-IR emission. Fig. 14 (b) shows that an error of less than an order of magnitude in the O_2 VD rates is able to cause the radiation discrepancy seen in the EX4 condition.

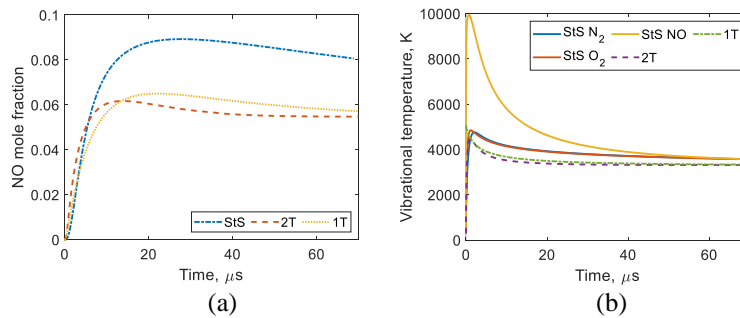


Fig. 12. Post-shock (a) NO mole fraction and (b) average vibrational temperature, from the state-to-state (StS), two-temperature (2T), and one-temperature (1T) simulations for the EX4 test case.

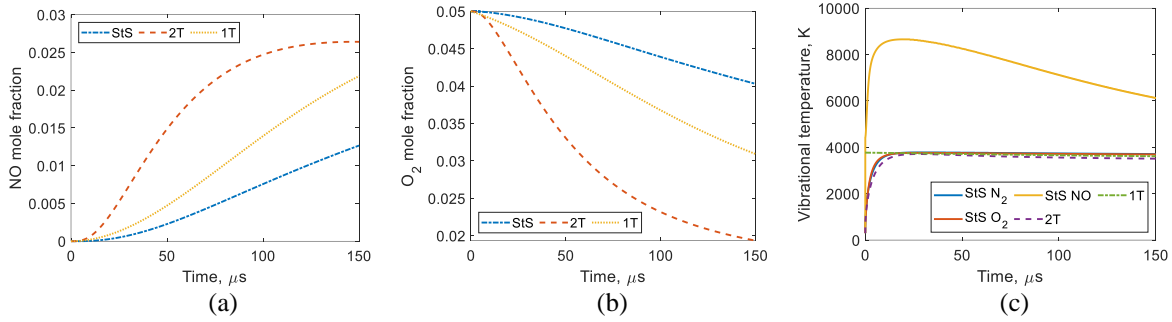


Fig. 13. Post-shock (a) NO mole fraction, (b) O₂ mole fraction and (c) average vibrational temperature, from the state-to-state (StS), two-temperature (2T), and one-temperature (1T) simulations for the EX3 test case.

The issue with the O₂ dissociation rate is manifested in a different way in the EX3 condition shown in Fig. 11 (g); a very slow radiation rise time is predicted by the StS model. As this improves with increasing O₂ content when comparing between EX1, EX2 and EX3 (Fig. 11 (a), (d) and (g) respectively), this is believed to indicate an issue with the O₂ dissociation rate with N₂ as the collision partner leading to a slow rate of production of oxygen atoms as shown by the mole fraction in Fig. 13 (b). This, in turn, causes a slow rate of production of NO as shown in Fig. 13 (a). Since the issue with the slow radiation rise time predicted by the StS model improves with increasing freestream velocity at the same mole fraction ratio of 0.95:0.05 as seen when comparing between EX3, EX6 and EX9 (Fig. 11 (g), (h) and (i) respectively), the aforementioned reaction may be particularly inaccurate at lower temperatures (less than 5000 K for the 3.0 km/s conditions). For the EX3 condition, an order of magnitude increase in the O₂ dissociation rate with N₂ is not even enough to correct the observed discrepancy as shown in Fig. 15. This reaction rate is calculated from FHO theory and extracted from the STELLAR database - no comparison has been made with first principles calculation and/or experiments for validation until now.

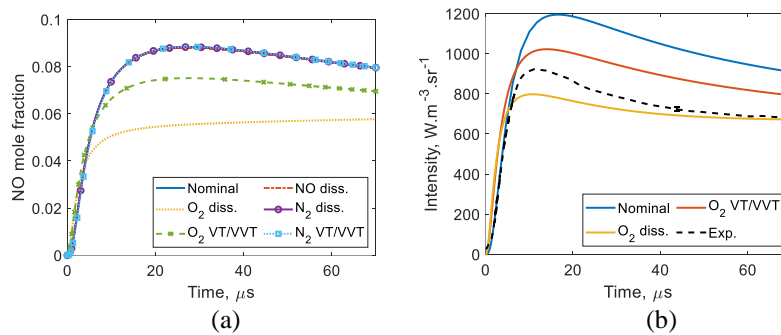


Fig. 14. The effect on the (a) NO mole fraction and (b) NO mid-IR radiation by increasing the various species dissociation and vibrational excitation rates by a factor of 10 in the StS model for the EX4 condition.

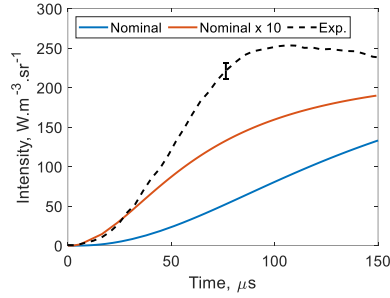


Fig. 15. The effect of increasing the $\text{O}_2(i) + \text{N}_2 \leftrightarrow 2\text{O} + \text{N}_2$ reaction rate in the StS model by a factor of 10 on the NO mid-IR emission.

One discrepancy feature which we do not have an explanation for from our parametric study is that shown in Fig. 11 (h) where the peak magnitude is predicted well by the StS model but the subsequent slope of the relaxation is much shallower compared to experiment. This is also mildly observable in the EX9 condition in Fig. 11 (i). Ref. [49] mentioned that boundary layer growth in the shock tube can potentially distort the time scale of the recorded profile. This could be an explanation for the discrepancy.

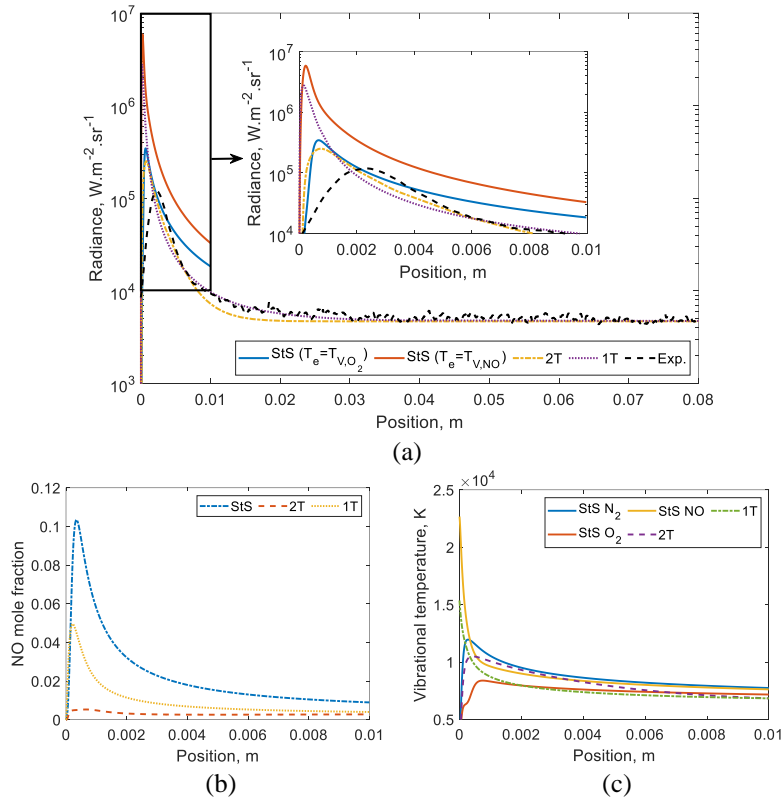


Fig. 16. Post-shock (a) 190 -280 nm integrated NO UV radiance, (b) NO mole fraction and (c) vibrational temperature, from the state-to-state (StS), two-temperature (2T), and one-temperature (1T) simulations for the 6.81 km/s test case. The experimental measurement of the UV radiance is also shown.

NO mid-IR emission measurements at velocities greater than 4.0 km/s are not available. However, shock tube emission measurements taken by NASA researchers for air at 190-1450 nm do exist for velocities between 7-9 km/s [52]. These emissions originate from various electronic transitions of various species, including the five species considered in this work. An attempt to simulate a 6.81 km/s shot ($p_\infty = 0.71$ torr and $T_\infty = 295$ K) using the current StS model was made and the results are shown in Fig. 16 (a) for the integrated emission between 190-280 nm which originate from the NO γ , β , β' , δ , ϵ , and γ' bands, with some contributions from the O₂ Schumann–Runge band and the N₂ second positive system. The experimental measurement along with the 1T and 2T results are also shown for comparison. Here, the emission is given in radiance and the self-absorption along the 10.16 cm (inner diameter) shock tube is accounted for. Of the set of experiments conducted by Ref. [52], only the lowest velocity case is considered because ionization and electronic excitation, which is not modelled in the current work, would become influential at higher velocities as discussed earlier. As the electronic mode is not modelled, the electronic level population is assumed to have a Boltzmann distribution according to the vibrational temperature for computing the radiance, which is a popular approximation [2, 12, 52].

Unfortunately, regarding the accuracy of the current vibrational state-specific model, the comparison in Fig. 16 (a) does not yield any meaningful information due to the high sensitivity of the emission to the population distribution in the electronic mode. The emission computed from the StS results can differ greatly depending on which vibrational temperature, Fig. 16 (c), is used to describe the electronic level population distribution even though the NO mole fraction (and NO number density) remains equal between the calculations. The differences are so large that a log scale has to be applied on the radiance axis in Fig. 16 (a). In turn, even though the StS NO mole fraction (Fig. 16 (b)) and number density is more than an order of magnitude larger than those of the 2T model, similar emissions are computed when the O₂ vibrational temperature is used for the StS result because the O₂ vibrational temperature is up to 5000 K lower than the 2T vibrational temperature. This is unlike the NO mid-IR emissions where the NO amount was shown to be more influential than the population distribution of the vibrational levels. The same trend was observed when assessing the emissions of electronic transitions from the other species and the same finding was obtained by Ref. [1, 2, 46] when attempting to simulate these emissions without modelling the electronic mode.

Recently, observations have been made that StS models predict significantly higher (close to an order of magnitude) peak NO mole fractions compared those predicted by Boltzmann models at high enthalpy conditions ($h_0 > 15$ MJ/kg), with the disagreement increasing with increasing h_0 [2, 8]. The same finding was made in the current

work and can be observed when comparing Fig. 12 (a) and Fig. 16 (b). This finding may not necessarily be a manifestation of the incorrect FHO dissociation rates postulated earlier. In Ref. [8], the same finding was made through heat bath simulations without VVT transitions using a completely independent set of state-specific rates generated entirely via the QCT method. They also performed the same simulations using a pure FHO rates model and good agreement in peak NO mole fraction was observed with the QCT results. It remains unresolved which model gives the correct NO mole fraction. The 2T model predicts the peak radiance well in magnitude (but not in location), and both Boltzmann models predict the radiance at position > 0.002 m remarkably well while the StS model over-predicts, as shown in Fig. 16 (a). However, due to the sensitivity of the UV radiance to the electronic level distribution, this may not necessarily indicate NO mole fractions of the Boltzmann models are correct because errors in the mole fractions would not be too noticeable in the UV radiance. Besides, a cancellation of errors from the electronic level distribution and NO mole fraction could in theory create the same observation.

VI. On the further development of the state-to-state model

As shown in Fig. 11 and even Fig. 16 (a), remarkably good predictions can be made by the Boltzmann models, which are better than the StS results in all cases. This raises a question: Why bother with the StS model if it is worse than the existing, low-fidelity models? The reason why further efforts should be devoted to the development of the StS model is because the StS model has potential to be significantly better than the Boltzmann models. The Boltzmann models are phenomenological models which involve various parameters which can be tuned to predict certain conditions. Consequently, the performance of these models is condition dependent with different parameters suitable for predicting different conditions. This can be observed in Fig. 11 where the 1T model is obviously better at predicting the EX9 condition (Fig. 11 (i)) while the 2T model is obviously better at predicting the EX2 condition (Fig. 11 (d)). On the other hand, the StS model is a proper physical model which means that it could potentially predict all relevant conditions without any parameter tuning. As mentioned earlier, the accuracy of state-specific simulations relies on the accuracy of the kinetic rates available. Therefore, further development of the StS model requires the generation and validation of all the relevant kinetic rates required for the state-specific simulation, which is a separate field of research. Regarding the validation of state-specific rates, the authors would like to make the following recommendations:

1. Validation of state-specific rates should be done by comparison with experimental data of thermochemical nonequilibrium flows;

2. To facilitate point 1, additional shock tube NO mid-IR emission measurements, like those taken by Ref. [49], should be made at varying $N_2:O_2$ mole fractions at higher velocities (> 4 km/s).

Regarding point 1, validation of state-specific rates is currently often done by comparing with other independently calculated rates, which is the same analysis presented in section III. Carried out less frequently, a more comprehensive assessment would be to implement the state-specific rates into a flow solver to perform simulations which could be compared with relevant experimental data, which is the analysis presented in section V. Validation of the rates are achieved when good agreement is found with the experimental results. In the case where discrepancies are observed, the characteristics of the discrepancies can be assessed to identify the problematic reactions. For example, the current work revealed that some of the O_2 dissociation rates may be inaccurate. Efforts can then be devoted to producing more accurate rates for these reactions.

Regarding point 2, while direct measurements of species mole fractions and excitation temperatures are ideal, these measurements are very difficult and comes with large uncertainties. The aforementioned NO mid-IR emission measurements are much easier to acquire and comes with a smaller uncertainty. This would certainly help address the large discrepancies observed in the peak NO mole fraction between the 2T and StS models, as discussed in section V. Additionally, experimentation with various $N_2:O_2$ composition allows for an assessment of the influences of different collision partners, as demonstrated in the current work. Unfortunately, NO is the only air species that produces significant radiation in the mid-IR region, which originate from ro-vibrational transitions. More species are found to radiate in the 190-1450 nm region as shown by NASA researchers [52]. However, radiation in this region originates from electronic transitions which is not useful for the validation of the current StS models as shown in section V. These measurements would be useful in the future once modelling of the kinetics of electronic excitation is included in the StS model (by means of a collisional-radiation model for example). However, such work should be done once an accurate vibrational state-specific model is obtained, which is not achieved at the moment even for low velocity conditions (< 4 km/s) as shown by the current study.

VII. Conclusions

A comprehensive StS model for air was formed - including VVT reactions for O_2-O_2 , N_2-N_2 , and O_2-N_2 . The VVT reaction rates were generated in this work using the FHO theory while most of the other reaction rates originated from either the FHO theory or first principles calculation. Comparison of the VVT FHO results to available SC and QCT results showed good agreement, especially at temperatures around 10,000 K and higher which are important for post-

shock nonequilibrium simulations. Using these VVT rates, the characteristics of the VVT transitions were assessed, looking at the influence of multi-quantum transitions and the influence of VV transitions, which are important for potentially reducing the number of VVT transitions. Three conditions were tested with velocities of 3.0, 5.0 and 7.0 km/s. Regarding the influence of multi-quantum transitions, restricting the quantum jumps to as small as 5 will predict the post-shock pressure, velocity, translational temperature and density profiles to within 3 % of the unrestricted result for all the tested conditions. On the other hand, much larger quantum jumps must be allowed if the vibrational population distribution of the high-lying energy levels of N_2 and O_2 needs to be simulated in the strong post-shock nonequilibrium region. Hence, the reduction on the number of VVT transitions possible depends on the application. The energy-based criterion for restricting VVT transitions was also tested and poorer results were obtained in all cases by this criterion when compared to the level-based criterion because this criterion prioritized reactions involving lower absolute rates. Regarding the influence of VV transitions, vibrational excitation becomes too fast if VVT transitions are reduced to VT transitions. This is observed in all three conditions and it is more severe for O_2 than for N_2 . This shows the importance of including VVT transitions in StS simulations.

To assess the performance of the current StS model and uncover any problematic rates, comparisons were made with the existing radiation emission measurements. Using NO mid-IR emissions from $u_\infty = 3.0 - 4.0$ km/s, it was revealed that some of the current O_2 dissociation rates may be inaccurate. At a higher velocity of 6.81 km/s, the NO mole fraction predicted by the StS model is around an order of magnitude greater than that predicted by the 2T model. No meaningful information could be obtained when comparing emissions originating from electronic transitions, which were the only ones available. Finally, recommendations were given on the further development of the StS model. In particular, 1) validation of state-specific rates should be done by comparison with experimental data of thermochemical nonequilibrium flows, and 2) additional shock tube NO mid-IR emission measurements should be made, at various $N_2:O_2$ mole fractions, at higher velocities (> 4 km/s).

Acknowledgments

The authors would like to acknowledge Qizhen Hong from the State Key Laboratory of High Temperature Gas Dynamics from the Institute of Mechanics at the Chinese Academy of Sciences for the helpful discussions. This work is supported by the Hong Kong Research Grants Council (no. 15206519).

References

1. Gimelshein, S. F., and Wysong, I. J. "Validation of high-temperature air reaction and relaxation models using emission data," *Journal of Thermophysics and Heat Transfer* Vol. 33, No. 3, 2019, pp. 606-616.
<https://doi.org/10.2514/1.T5555>
2. Su, W., Bruno, D., and Babou, Y. "State-specific modeling of vibrational relaxation and nitric oxide formation in shock-heated air," *Journal of Thermophysics and Heat Transfer* Vol. 32, No. 2, 2018, pp. 337-352.
<https://doi.org/10.2514/1.T5271>
3. Andrienko, D., and Boyd, I. D. "Investigation of oxygen vibrational relaxation by quasi-classical trajectory method," *Chemical Physics* Vol. 459, 2015, pp. 1-13.
<https://doi.org/10.1016/j.chemphys.2015.07.023>
4. Borges Sebastião, I., Kulakhmetov, M., and Alexeenko, A. "DSMC study of oxygen shockwaves based on high-fidelity vibrational relaxation and dissociation models," *Physics of Fluids* Vol. 29, No. 1, 2017, p. 017102.
<https://doi.org/10.1063/1.4974056>
5. Kim, J. G., and Boyd, I. D. "State-resolved master equation analysis of thermochemical nonequilibrium of nitrogen," *Chemical Physics* Vol. 415, 2013, pp. 237-246.
<https://doi.org/10.1016/j.chemphys.2013.01.027>
6. Panesi, M., Munafò, A., Magin, T., and Jaffe, R. "Nonequilibrium shock-heated nitrogen flows using a rovibrational state-to-state method," *Physical Review E* Vol. 90, No. 1, 2014, p. 013009.
<https://doi.org/10.1103/PhysRevE.90.013009>
7. Wysong, I., Gimelshein, S., Bondar, Y., and Ivanov, M. "Comparison of direct simulation Monte Carlo chemistry and vibrational models applied to oxygen shock measurements," *Physics of Fluids* Vol. 26, No. 4, 2014, p. 043101.
<https://doi.org/10.1063/1.4871023>
8. Fangman, A. J., and Andrienko, D. "A state-to-state and multi-temperature study of air thermochemistry," *AIAA Scitech 2021 Forum*. AIAA Paper 2021-0316, January 2021.
<https://doi.org/10.2514/6.2021-0316>
9. Lino da Silva, M., Loureiro, J., and Guerra, V. "A multiquantum dataset for vibrational excitation and dissociation in high-temperature O₂-O₂ collisions," *Chemical Physics Letters* Vol. 531, 2012, pp. 28-33.
<https://doi.org/10.1016/j.cplett.2012.01.074>
10. Lino da Silva, M., Guerra, V., and Loureiro, J. "State-resolved dissociation rates for extremely nonequilibrium atmospheric entries," *Journal of thermophysics and heat transfer* Vol. 21, No. 1, 2007, pp. 40-49.
<https://doi.org/10.2514/1.24114>
11. Strand, J. S., and Goldstein, D. B. "Global sensitivity analysis for DSMC simulations of hypersonic shocks," *Journal of Computational Physics* Vol. 246, 2013, pp. 184-206.
<https://doi.org/10.1016/j.jcp.2013.03.035>
12. Park, C. "Review of chemical-kinetic problems of future NASA missions. I-Earth entries," *Journal of Thermophysics and Heat transfer* Vol. 7, No. 3, 1993, pp. 385-398.
<https://doi.org/10.2514/3.431>
13. Esposito, F., Armenise, I., and Capitelli, M. "N-N₂ state to state vibrational-relaxation and dissociation rates based on quasiclassical calculations," *Chemical Physics* Vol. 331, No. 1, 2006, pp. 1-8.
<https://doi.org/10.1016/j.chemphys.2006.09.035>
14. Esposito, F., and Capitelli, M. "The relaxation of vibrationally excited O₂ molecules by atomic oxygen," *Chemical physics letters* Vol. 443, No. 4-6, 2007, pp. 222-226.
<https://doi.org/10.1016/j.cplett.2007.06.099>
15. Bose, D., and Candler, G. V. "Thermal rate constants of the N₂+ O → NO+ N reaction using ab initio 3 A' and 3 A' potential energy surfaces," *The Journal of chemical physics* Vol. 104, No. 8, 1996, pp. 2825-2833.
<https://doi.org/10.1063/1.471106>

16. Bose, D., and Candler, G. V. "Thermal rate constants of the $O_2 + N \rightarrow NO + O$ reaction based on the $A^2 \Sigma^+$ and $A^4 \Sigma^+$ potential-energy surfaces," *The Journal of chemical physics* Vol. 107, No. 16, 1997, pp. 6136-6145.
<https://doi.org/10.1063/1.475132>
17. Lino da Silva, M., Lopez, B., Guerra, V., and Loureiro, J. "A multiquantum state-to-state model for the fundamental states of air: the stellar database," *Proceedings of 5th International Workshop Radiation of High Temperature Gases in Atmospheric Entry*. Vol. 714, ESASP, Ouweland, 2012, p. 16.
18. Luo, H., Kulakhmetov, M., and Alexeenko, A. "Ab initio state-specific $N_2 + O$ dissociation and exchange modeling for molecular simulations," *The Journal of chemical physics* Vol. 146, No. 7, 2017, p. 074303.
<https://doi.org/10.1063/1.4975770>
19. Esposito, F., and Armenise, I. "Reactive, inelastic, and dissociation processes in collisions of atomic oxygen with molecular nitrogen," *The Journal of Physical Chemistry A* Vol. 121, No. 33, 2017, pp. 6211-6219.
<https://doi.org/10.1021/acs.jpca.7b04442>
20. Esposito, F., and Armenise, I. "Reactive, Inelastic, and Dissociation Processes in Collisions of Atomic Nitrogen with Molecular Oxygen," *The Journal of Physical Chemistry A* Vol. 125, No. 18, 2021, pp. 3953-3964.
<https://doi.org/10.1021/acs.jpca.0c09999>
21. Jaffe, R. L., Schwenke, D. W., and Panesi, M. "First principles calculation of heavy particle rate coefficients," *Hypersonic Nonequilibrium Flows: Fundamentals and Recent Advances*. Vol. 247, American Institute of Aeronautics and Astronautics, 2015, pp. 103-158.
22. Adamovich, I. V., Macheret, S. O., Rich, J. W., and Treanor, C. E. "Vibrational energy transfer rates using a forced harmonic oscillator model," *Journal of Thermophysics and Heat Transfer* Vol. 12, No. 1, 1998, pp. 57-65.
<https://doi.org/10.2514/2.6302>
23. Adamovich, I. V., Macheret, S. O., Rich, J. W., and Treanor, C. E. "Vibrational relaxation and dissociation behind shock waves. Part 1-Kinetic rate models," *AIAA journal* Vol. 33, No. 6, 1995, pp. 1064-1069.
<https://doi.org/10.2514/3.12528>
24. Zelechow, A., Rapp, D., and Sharp, T. E. "Vibrational-vibrational-translational energy transfer between two diatomic molecules," *The Journal of Chemical Physics* Vol. 49, No. 1, 1968, pp. 286-299.
<https://doi.org/10.1063/1.1669823>
25. Hao, J., Wang, J., and Lee, C. "State-specific simulation of oxygen vibrational excitation and dissociation behind a normal shock," *Chemical Physics Letters* Vol. 681, 2017, pp. 69-74.
<https://doi.org/10.1016/j.cplett.2017.05.042>
26. Vargas, J. o., Lopez, B., and Lino da Silva, M. r. "Heavy Particle Impact Vibrational Excitation and Dissociation Processes in CO_2 ," *The Journal of Physical Chemistry A* Vol. 125, No. 2, 2021, pp. 493-512.
<https://doi.org/10.1021/acs.jpca.0c05677>
27. Lopez, B., and Lino Da Silva, M. "Non-Boltzmann analysis of hypersonic air re-entry flows," *11th AIAA/ASME Joint Thermophysics and Heat Transfer Conference*. AIAA Paper 2014-2547, June 2014.
<https://doi.org/10.2514/6.2014-2547>
28. Hao, J., Wang, J., and Lee, C. "Assessment of vibration-dissociation coupling models for hypersonic nonequilibrium simulations," *Aerospace Science and Technology* Vol. 67, 2017, pp. 433-442.
<https://doi.org/10.1016/j.ast.2017.04.027>
29. Hao, J., and Wen, C.-Y. "Effects of vibrational nonequilibrium on hypersonic shock-wave/laminar boundary-layer interactions," *International Communications in Heat and Mass Transfer* Vol. 97, 2018, pp. 136-142.
<https://doi.org/10.1016/j.icheatmasstransfer.2018.07.010>
30. Aliat, A., Vedula, P., and Josyula, E. "Simple model for vibration-translation exchange at high temperatures: Effects of multiquantum transitions on the relaxation of a N_2 gas flow behind a shock," *Physical Review E* Vol. 83, No. 2, 2011, p. 026308.
<https://doi.org/10.1103/PhysRevE.83.026308>

31. Aliat, A., Vedula, P., and Josyula, E. "State-specific dissociation modeling with multiquantum vibration-translation transitions," *Physical Review E* Vol. 83, No. 3, 2011, p. 037301.
<https://doi.org/10.1103/PhysRevE.83.037301>
32. Park, C. "Thermochemical relaxation in shock tunnels," *Journal of thermophysics and heat transfer* Vol. 20, No. 4, 2006, pp. 689-698.
<https://doi.org/10.2514/1.22719>
33. Billing, G. D., and Kolesnick, R. "Vibrational relaxation of oxygen. State to state rate constants," *Chemical Physics Letters* Vol. 200, No. 4, 1992, pp. 382-386.
[https://doi.org/10.1016/0009-2614\(92\)87008-D](https://doi.org/10.1016/0009-2614(92)87008-D)
34. Coletti, C., and Billing, G. D. "Vibrational energy transfer in molecular oxygen collisions," *Chemical physics letters* Vol. 356, No. 1-2, 2002, pp. 14-22.
[https://doi.org/10.1016/S0009-2614\(02\)00279-8](https://doi.org/10.1016/S0009-2614(02)00279-8)
35. Hong, Q., Sun, Q., Pirani, F., Valentín-Rodríguez, M. A., Hernández-Lamoneda, R., Coletti, C., Hernández, M. I., and Bartolomei, M. "Energy exchange rate coefficients from vibrational inelastic O₂ (Σ g⁻ 3)+ O₂ (Σ g⁻ 3) collisions on a new spin-averaged potential energy surface," *The Journal of Chemical Physics* Vol. 154, No. 6, 2021, p. 064304.
<https://doi.org/10.1063/5.0041244>
36. Ormonde, S. "Vibrational relaxation theories and measurements," *Reviews of Modern Physics* Vol. 47, No. 1, 1975, pp. 193-258.
<https://doi.org/10.1103/RevModPhys.47.193>
37. Billing, G. D., and Fisher, E. "VV and VT rate coefficients in N₂ by a quantum-classical model," *Chemical Physics* Vol. 43, No. 3, 1979, pp. 395-401.
[https://doi.org/10.1016/0301-0104\(79\)85207-6](https://doi.org/10.1016/0301-0104(79)85207-6)
38. Hong, Q., Sun, Q., Bartolomei, M., Pirani, F., and Coletti, C. "Inelastic rate coefficients based on an improved potential energy surface for N₂+ N₂ collisions in a wide temperature range," *Physical Chemistry Chemical Physics* Vol. 22, No. 17, 2020, pp. 9375-9387.
<https://doi.org/10.1039/D0CP00364F>
39. Billing, G. D. "VV and VT rates in N₂-O₂ collisions," *Chemical physics* Vol. 179, No. 3, 1994, pp. 463-467.
[https://doi.org/10.1016/0301-0104\(94\)87022-5](https://doi.org/10.1016/0301-0104(94)87022-5)
40. Garcia, E., Kurnosov, A., Laganà, A., Pirani, F., Bartolomei, M., and Cacciatore, M. "Efficiency of collisional O₂+ N₂ vibrational energy exchange," *The Journal of Physical Chemistry B* Vol. 120, No. 8, 2016, pp. 1476-1485.
<https://doi.org/10.1021/acs.jpcc.5b06423>
41. Andrienko, D., and Boyd, I. D. "Master equation simulation of O₂-N₂ collisions on an ab-initio potential energy surface," *47th AIAA Thermophysics Conference*. AIAA paper 2017-3163, June 2017.
<https://doi.org/10.2514/6.2017-3163>
42. Andrienko, D. A., and Boyd, I. D. "Kinetic models of oxygen thermochemistry based on quasi-classical trajectory analysis," *Journal of Thermophysics and Heat Transfer* Vol. 32, No. 4, 2018, pp. 904-916.
<https://doi.org/10.2514/1.T4968>
43. Taylor, R. L., and Bitterman, S. "Survey of Vibrational Relaxation Data for Processes Important in the CO₂-N₂ Laser System," *Reviews of Modern Physics* Vol. 41, No. 1, 1969, pp. 26-47.
<https://doi.org/10.1103/RevModPhys.41.26>
44. Ozbenli, E., Vedula, P., Vogiatzis, K., and Josyula, E. "Numerical solution of hypersonic flows via artificial neural networks," *AIAA Scitech 2020 Forum*. AIAA Paper 2020-1233, January 2020.
<https://doi.org/10.2514/6.2020-1233>
45. Bose, D., and Candler, G. V. "Simulation of hypersonic flows using a detailed nitric oxide formation model," *Physics of Fluids* Vol. 9, No. 4, 1997, pp. 1171-1181.
<https://doi.org/10.1063/1.869205>

46. Campoli, L., Kunova, O., Kustova, E., and Melnik, M. "Models validation and code profiling in state-to-state simulations of shock heated air flows," *Acta Astronautica* Vol. 175, 2020, pp. 493-509.
<https://doi.org/10.1016/j.actaastro.2020.06.008>
47. Grover, M. S., Valentini, P., Josyula, E., and Chaudhry, R. S. "Vibrational state-to-state and multiquantum effects for N₂⁺ N₂ interactions at high temperatures for aerothermodynamic applications," *AIAA Scitech 2020 Forum*. AIAA Paper 2020-1227, January 2020.
<https://doi.org/10.2514/6.2020-1227>
48. Wurster, W., Treanor, C., and Williams, M. "Non-equilibrium radiation from shock-heated air." Calspan, Univ. of Buffalo Research Center Final Rept. 92-00426, Buffalo, NY, 1991.
49. Treanor, C. E., and Williams, M. J. "Kinetics of Nitric Oxide Formation Behind 3 to 4 km/s Shock Waves." Calspan, Univ. of Buffalo Research Center Final Rept. 93-09744, Buffalo, NY, February 1993.
50. Gupta, R. N., Yos, J. M., Thompson, R. A., and Lee, K.-P. "A review of reaction rates and thermodynamic and transport properties for an 11-species air model for chemical and thermal nonequilibrium calculations to 30000 K." Langley Research Center NASA STI/Recon Technical Report NASA-RP-1232, Hampton, VA., 1990.
51. Lino da Silva, M. "SPARK Line-by-Line v.3.0 User Manual." Institute of Plasmas and Nuclear Fusion, Instituto Superior Técnico, Lisbon, 2021.
52. Cruden, B. A., and Brandis, A. M. "Measurement and prediction of radiative non-equilibrium for air shocks between 7-9 km/s," *47th AIAA Thermophysics Conference*. AIAA Paper 2017-4535, June 2017.
<https://doi.org/10.2514/6.2017-4535>
53. Andrienko, D. A., and Boyd, I. D. "State-specific dissociation in O₂-O₂ collisions by quasiclassical trajectory method," *Chemical Physics* Vol. 491, 2017, pp. 74-81.
<https://doi.org/10.1016/j.chemphys.2017.05.005>